Wavelength-Dependent Photolysis of *n*-Hexanal and *n*-Heptanal in the 280−330-nm Region

Yongxin Tang and Lei Zhu*

Wadsworth Center, New York State Department of Health, Department of Environmental Health and Toxicology, State University of New York, Albany, New York 12201-0509

Received: May 7, 2004; In Final Form: July 16, 2004

We have studied the photolysis of *n*-hexanal ($CH_3(CH_2)_4CHO$) and *n*-heptanal ($CH_3(CH_2)_5CHO$) at 5-nm intervals in the 280−330-nm region by using dye-laser photolysis combined with cavity ring-down spectroscopy. Their absorption cross sections have been obtained at each wavelength studied. The HCO radical is a photodissociation product of both aldehydes. The HCO radical quantum yields have been determined as a function of photolysis wavelength (λ), aldehyde pressure, and nitrogen buffer gas pressure. The HCO radical yields decrease with increasing aldehyde pressure (0.5−8 Torr for *n*-hexanal and 0.5−4 Torr for *n*-heptanal) because of the increasing HCO + HCO, HCO + R, and HCO + RCHO reactions (R = *n*-C_5H_{11} for *n*-hexanal and *n*-C_6H_{13} for *n*-heptanal) at higher aldehyde pressures and because of quenching by ground-state aldehydes. After separating the contribution of HCO radical reactions, the aldehyde-pressure quenching effect was still observed at all wavelengths. The HCO quantum yields and the ratios of quenching to unimolecular decay rate constants of excited aldehydes are given. The HCO quantum yields from *n*-hexanal photolysis are 0.12 ± 0.01, 0.15 ± 0.02, 0.14 ± 0.02, and 0.10 ± 0.01 at 305, 310, 315, and 320 nm, respectively, where the uncertainty (1σ) represents experimental scatter. The corresponding HCO quantum yields from *n*-heptanal photolysis are 0.14 ± 0.04, 0.15 ± 0.06, 0.10 ± 0.01, and 0.11 ± 0.02, respectively. A comparison of the HCO radical yields from the wavelength-dependent photolysis of *n*-hexanal and *n*-heptanal with that from *n*-pentanal photolysis indicates that the HCO radical yields from aldehyde photolysis do not vary with chain length for aldehydes with chain lengths that are longer than or equal to five carbon atoms. The dependence of the HCO quantum yield on nitrogen buffer gas pressure was examined between 6 and 387 Torr; no dependence was observed. The end products from 308-nm excimer-laser photolysis of both aldehydes were measured by mass spectrometry and FTIR. Evidence has been obtained for the occurrence of the Norrish II channel, and the photocyclization channels for both aldehydes and their yields have been obtained.

Introduction

The atmospheric chemistry of aliphatic aldehydes has been studied extensively as a result of their important role in the formation of photochemical smog, peroxyacetyl nitrate (PAN), and ground-level ozone.[1,2] The photodissociation of aldehydes has received special attention because it is an important source of free radicals in the atmosphere.[3] The photolysis of C1−C5 aldehydes has been studied previously.[4−10] Our group recently investigated the wavelength-dependent photolysis of propanal (C_2H_5CHO), *n*-butanal (*n*-C_3H_7CHO), and *n*-pentanal (*n*-C_4H_9CHO) in the 280−330-nm region.[8−10] Our study indicates that the peak HCO quantum yields from aldehyde photolysis decrease with aldehyde chain length as a result of the opening of the Norrish II channel for *n*-butanal and *n*-pentanal. (The peak HCO yields are 1.08 ± 0.07, 0.84 ± 0.04, and 0.20 ± 0.06 for propanal, *n*-butanal, and *n*-pentanal, respectively.) It would be interesting to examine whether the radical yields will continue to decrease with alkyl chain length for longer chain aldehydes such as *n*-hexanal ($CH_3(CH_2)_4CHO$) and *n*-heptanal ($CH_3(CH_2)_5CHO$). The major sources of *n*-hexanal and *n*-heptanal in natural environments are direct emissions from forests (0.09−1.8 ppbv for *n*-hexanal and 0.07−2.1 ppbv for *n*-heptanal),[11,12] pastures (*n*-hexanal constituted 3−4% of total carbon emission from grass with midday emission flux for grass of approximately 3200 μg(C) m^{-2} h^{-1}),[13] crop harvesting (the emission flux of *n*-hexanal plus (*E*)-2-hexenol was about 1800−2412 μg m^{-2} h^{-1}),[14] lawn mowing (concentrations of *n*-hexanal plus hexenols were on the order of 1−7 ppbv),[15] and leaves after freeze−thaw wounding (0.8−4 ppbv for *n*-hexanal).[16] In polluted airsheds, *n*-hexanal and *n*-heptanal are emitted directly from light-duty and heavy-duty vehicles (0.20−1.71 μg m^{-3} for *n*-hexanal and 2.63−0.11 μg m^{-3} for *n*-heptanal),[17,18] from fireplace combustion of wood (90−418 mg of *n*-hexanal per kg of wood burned and 77−626 mg of *n*-heptanal per kg of wood burned),[19] and from frying vegetables in seed oils (4.1−6.7 mg of *n*-hexanal per kg of vegetables cooked and 4.3−8.0 mg of *n*-heptanal per kg of vegetables cooked)[20] and are products from the gas-phase ozonolysis of alkenes.[21−23] There has been an end-product study of the broadband oxidation of *n*-hexanal in air over the 275−380-nm range.[24] The yields of the Norrish II channel at 254 and 312 nm were obtained by monitoring the 1-butene product from the photolysis of *n*-hexanal.[25] The photolysis of *n*-heptanal has been investigated by combining an emission lamp (275−380 nm) with FTIR.[26] The determination of the wavelength-dependent photolysis yields of *n*-hexanal and *n*-heptanal allows a comparison with our earlier results from the photolysis of *n*-butanal[9] and *n*-pentanal[10] and allows for the establishment of the relationship between radical yields and aldehyde alkyl chain length. It also permits an estimate of their tropospheric radical formation rate constants.

* Author to whom correspondence should be addressed. E-mail: zhul@wadsworth.org. Tel: 518-474-6846. Fax: 518-473-2895.

10.1021/jp0403442 CCC: $27.50
Published on Web 09/08/2004

n-Hexanal and *n*-heptanal exhibit a weak UV absorption band in the 240−360-nm region as a result of a symmetry-forbidden n → π^* transition.[27] The thermodynamically allowed dissociation pathways following the excitation of *n*-hexanal and *n*-heptanal in the UV region are as follows

$$\mathrm{RCHO} + h\nu \rightarrow \mathrm{R} + \mathrm{HCO}\ (\lambda \leq 339\ \mathrm{nm\ for\ R} = n\text{-}\mathrm{C_5H_{11}}\ \mathrm{and}\ n\text{-}\mathrm{C_6H_{13}}) \quad (1)$$

$$\rightarrow \mathrm{RH} + \mathrm{CO}\ (\mathrm{all}\ \lambda) \quad (2)$$

$$\rightarrow \mathrm{R'H} + [\mathrm{CH_2{=}CHOH}] \leftrightarrow \mathrm{R'H} + \mathrm{CH_3CHO}\ (\lambda \leq 978\ \mathrm{nm\ for\ R'} = \mathrm{C_4H_7}\ \mathrm{and}\ \mathrm{C_5H_9}) \quad (3)$$

$$\rightarrow \mathrm{RCO} + \mathrm{H}\ (\lambda \leq 306\ \mathrm{nm\ for\ R} = n\text{-}\mathrm{C_5H_{11}}\ \mathrm{and}\ n\text{-}\mathrm{C_6H_{13}}) \quad (4)$$

$$\rightarrow \text{2-methylcyclo-R''-OH}\ (\lambda \leq 1.3\ \mu\mathrm{m\ for\ R''} = \mathrm{C_5H_8}\ \mathrm{and}\ \mathrm{C_6H_{10}}) \quad (5)$$

$$\rightarrow \text{2-ethylcyclo-R}^{\mathrm{III}}\text{-OH}\ (\lambda \leq 1.3\ \mu\mathrm{m\ for\ R^{III}} = \mathrm{C_4H_6}\ \mathrm{and}\ \mathrm{C_5H_8}) \quad (6)$$

where threshold wavelengths were calculated from the corresponding enthalpy changes. Photolysis channels 1, 2, and 3 are radical-formation, molecular-elimination, and Norrish II channels, respectively. Channel 4 is another radical-formation channel but was found to be minor for aliphatic aldehydes.[28] Channels 5 and 6 are photocyclization channels, and they are available for $\geq C_5$ aldehydes.

We present in this paper results obtained from an experimental study of the photolysis of *n*-hexanal and *n*-heptanal at 5-nm intervals in the 280−330-nm region using dye-laser photolysis combined with the cavity ring-down technique.[29,30] Absorption cross sections of *n*-hexanal and *n*-heptanal have been obtained at each wavelength studied. The quantum yields of HCO from the photolysis of both aldehydes and their dependence on photolysis wavelength, aldehyde pressure, and nitrogen buffer gas pressure have been acquired. The absolute HCO radical concentration was calibrated relative to that obtained from the photolysis of formaldehyde, HCHO + $h\nu$ → H + HCO, for which the recommended HCO radical yield at each photolysis wavelength is available.[31] The end products from 308-nm excimer-laser photolysis of *n*-hexanal and *n*-heptanal have been identified with mass spectrometry and FTIR, and their corresponding yields have been obtained. Radical formation rate constants from the photolysis of *n*-hexanal and *n*-heptanal have been estimated as a function of the zenith angle for cloudless conditions at sea level and at 760 Torr nitrogen pressure.

Experimental Techniques

The experimental setup has been described in detail previously.[10,32−34] Two laser systems were employed in this work. One was used to photolyze aldehydes, and the other was used to probe the HCO radical product. The second-harmonic output of a tunable dye laser pumped by a 308-nm XeCl excimer laser (∼200 mJ/pulse, Lambda Physik) was used as photolysis radiation. Laser dyes used in the experiments included coumarin 153, rhodamine 6G, rhodamine B, rhodamine 101, and DCM. The photolysis laser beam was introduced into the reaction cell at a 15° angle to the main cell axis through a sidearm. The probe laser beam (613−617 nm, ∼0.1 mJ/pulse, 0.01-nm laser bandwidth) from a dye laser pumped by a nitrogen laser (Laser Photonics) was directed along the main optical axis of the cell.

TABLE 1: Absorption Cross Sections of *n*-Hexanal and *n*-Heptanal as a Function of Wavelength

λ (nm)	σ (*n*-hexanal) (10^{-20} cm^2 molecule^{-1})	σ (*n*-heptanal) (10^{-20} cm^2 molecule^{-1})
280	5.45 ± 0.13	5.44 ± 0.33
285	6.13 ± 0.19	6.39 ± 0.82
290	6.04 ± 0.19	5.99 ± 0.41
295	6.45 ± 0.18	6.62 ± 0.43
300	5.94 ± 0.25	5.61 ± 0.19
305	5.61 ± 0.24	5.29 ± 0.41
310	4.38 ± 0.18	4.72 ± 0.34
315	3.75 ± 0.27	3.99 ± 0.29
320	2.51 ± 0.13	2.94 ± 0.28
325	1.96 ± 0.23	1.85 ± 0.31
330	1.23 ± 0.16	1.06 ± 0.21

The pump and the probe laser beams crossed one another at the center of the reaction cell, which was vacuum sealed with a pair of high-reflectance cavity mirrors. The base path length between the two cavity mirrors was 50 cm. A fraction of the probe laser pulse was injected into the cavity through the front mirror, and its intensity decayed as the light bounced back and forth inside the cell. The light-intensity decay inside the cavity was measured by monitoring the weak transmission of light through the rear mirror with a photomultiplier tube (PMT). The PMT output was amplified, digitized, and sent to a computer. The decay curve was fit to a single-exponential decay function. The ring-down time constant and the total loss per optical pass were calculated. The ring-down time constant was on the order of 31 μs for an empty cavity, with about a 53 ppm transmission loss per mirror. In the presence of absorbing species, the cavity decay time shortened. By measuring the cavity losses with and without a photolysis pulse, the HCO absorption from the photolysis of *n*-hexanal and *n*-heptanal was obtained. A pulse/decay generator was used to vary the delay time between the firing of the photolysis and the probe lasers. The photolysis laser pulse energy was measured with a calibrated joulemeter (Molectron). Gas pressure was measured at the center of the reaction cell with an MKS Baratron capacitance manometer. Quantum yield measurements were made at a repetition rate of 0.1 Hz to ensure the replenishment of the gas samples between successive laser pulses. The spectrum scan was performed at a laser repetition rate of 1 Hz. All experiments were carried out at an ambient temperature of 293 ± 2 K.

The mass spectra of the stable end products from the photolysis of *n*-hexanal and *n*-heptanal were taken with a residual gas analyzer mass spectrometer (RGA300, Stanford Research Systems) connected online with the photolysis cell. An FTIR spectrometer (IFS 66v, Bruker Optics) was also used to characterize photolysis end products.

n-Hexanal (≥ 98% purity, Aldrich) and *n*-heptanal (≥ 95% purity, Aldrich) were purified by repeated freeze−pump−thaw cycles at 77 K before each experiment to remove volatile impurities. The purity of both aldehydes was checked by FTIR, and no impurities were found. Formaldehyde was generated by the pyrolysis of paraformaldehyde (≥ 95% purity, Aldrich) at 110 °C. Nitrogen (≥ 99.999% purity, BOC Edwards) was used without further purification.

Results and Discussion

Absorption Cross Sections of *n*-Hexanal and *n*-Heptanal in the 280−330 nm Region. The room-temperature absorption cross sections of *n*-hexanal and *n*-heptanal have been determined at 5-nm intervals in the 280−330-nm region. They are listed in Table 1 and plotted in Figure 1. The absorption cross section

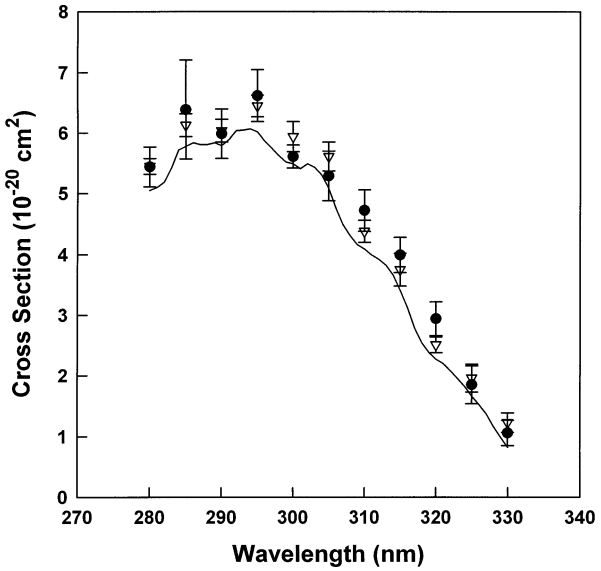

Figure 1. Absorption cross sections of *n*-hexanal (▽) and *n*-heptanal (●) in the 280−330-nm region. The solid line represents literature cross-sectional data of *n*-hexanal.[24]

at each wavelength was obtained by monitoring the intensity of the transmitted photolysis beam as a function of *n*-hexanal or *n*-heptanal pressure in the cell and by applying Beer's law to the experimental data. The room-temperature vapor pressures of *n*-hexanal and *n*-heptanal are about 8.5 and 2.3 Torr, respectively. The error bars that are quoted (1σ) are the estimated precision of cross-section determinations, which include the standard deviation for each measurement plus the standard deviation about the mean of at least six repeated experimental runs. Besides random errors, systematic errors also contribute to the uncertainty in cross-section values. The major sources of systematic errors are those involving pressure and path-length determinations and those resulting from the presence of impurities in the samples. Adding relative (shown in Table 1) and systematic errors, the overall uncertainty for *n*-hexanal cross-section measurements is about 5−8% in the 280−310-nm range and at 320 nm, 10% at 315 nm, and 15−16% at 325 and 330 nm. The overall uncertainty for *n*-heptanal cross-section measurements is about 9% at 300 nm, 12−16% at 280, 290, and 295 nm and in the 305−320 nm range, 19% at 285 nm, 23% at 325 nm, and 26% at 330 nm. As seen from Figure 1, the cross-section values of *n*-hexanal are similar to those of *n*-heptanal. For the purpose of comparison, the literature *n*-hexanal cross-section values by Tadic and co-workers[24] are also shown in Figure 1. Absorption cross sections of *n*-heptanal have not been reported previously. Our cross-section values for *n*-hexanal agree with literature values to within 5% at 290 nm, 10% at 280, 285, 295, 300, 305, 310, 315, and 320 nm, 15% at 325 nm, and 35% at 330 nm. The differences between our *n*-hexanal cross-section values and those of the previous study are small but systematic. Our cross-section measurement was based upon the determination of the transmitted photolysis laser fluence as a function of *n*-hexanal pressure in the cell. If there was a slight drop in dye-laser fluence during our cross-section measurements, then it would translate into systematic measurement uncertainty, which made our cross-section values larger than the real values.

Time-Resolved Studies of the Photolysis of *n*-Hexanal and *n*-Heptanal in the 280−330-nm Region. Presented in Figure 2 is a cavity ring-down absorption spectrum of the product after 280-nm photolysis of *n*-hexanal. Also shown in the same Figure is a previously reported absorption spectrum of HCO in the same

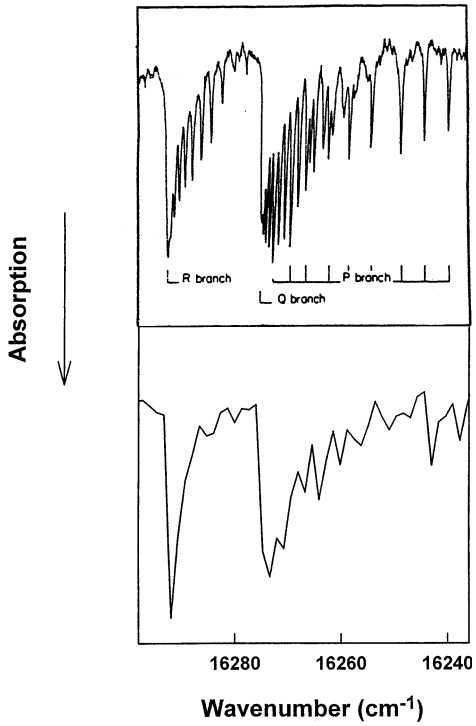

Figure 2. (Top) Intracavity laser absorption spectrum of the (000) → (090) vibronic transition of HCO following the photolysis of 0.1 Torr CH_3CHO/10 Torr Ar at 266 nm (adapted from ref 35). (Bottom) Low-resolution cavity ring-down absorption spectrum of the product from the photolysis of *n*-hexanal at 280 nm. The spectrum was taken at a wavelength interval of 0.05 nm.

wavelength region.[35] A comparison of these two spectra indicates that the HCO radical is a photolysis product of *n*-hexanal. A similar product absorption spectrum was also obtained from the photolysis of *n*-heptanal. The cavity ring-down spectrometer was tuned to the HCO X^2A'' (0, 0, 0) → A^2A' (0, 9, 0) R bandhead at 613.8 nm (spectral bandwidth ~2.5 cm^{-1}; measured $\sigma_{HCO} \approx 2.0 \times 10^{-18}$ cm^2), and the HCO concentration was followed as a function of time. Shown in Figure 3 is a transient profile of HCO from the 280-nm photolysis of 8 Torr *n*-hexanal along with a fit of the HCO decay profile using the following kinetic scheme

$$\mathrm{HCO} + \mathrm{HCO} \rightarrow \mathrm{HCHO} + \mathrm{CO} \quad (7)$$

$$\mathrm{HCO} + n\text{-}\mathrm{C_5H_{11}} \rightarrow \text{products} \quad (8)$$

$$\mathrm{HCO} + n\text{-}\mathrm{C_5H_{11}CHO} \rightarrow \text{products} \quad (9)$$

$$n\text{-}\mathrm{C_5H_{11}} + n\text{-}\mathrm{C_5H_{11}} \rightarrow \text{products} \quad (10)$$

$$n\text{-}\mathrm{C_5H_{11}} \rightarrow \text{products} \quad (11)$$

This modeling scheme assumes that n-C_5H_{11} + HCO is the only important radical-formation channel from the photolysis of *n*-hexanal at 280 nm. (As described later, the HCO quantum yield from the photolysis of *n*-hexanal at 280 nm is 0.073, and the balance of the yield is attributed to contributions from the Norrish II channel (CH_3CHO + C_4H_8), the photocyclization channels, and the molecular elimination channel (CO + C_5H_{12}).) Time profiles of HCO from the photolysis of 4, 6, and 8 Torr *n*-hexanal were compared with the values calculated by the ACUCHEM simulation program.[36] The following input parameters were used: rate constants for the HCO + HCO, HCO + n-C_5H_{11}, HCO + n-$C_5H_{11}CHO$, n-C_5H_{11} + n-C_5H_{11}, and the unimolecular n-C_5H_{11} isomerization reactions ($k_{HCO+HCO}$,

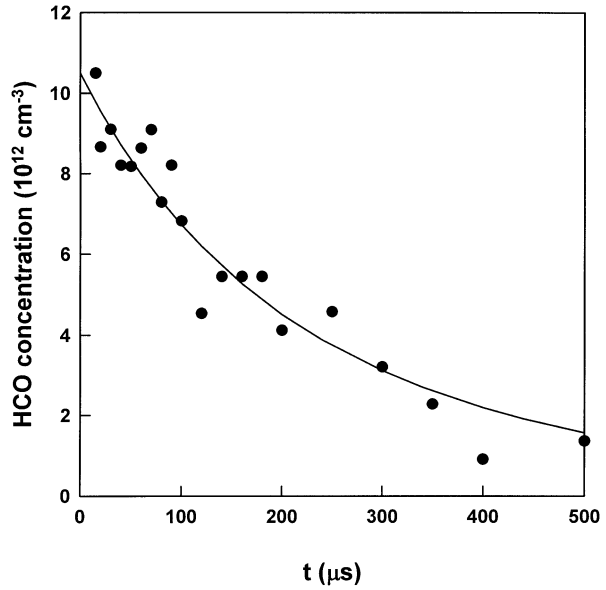

Figure 3. Time profile of the HCO radical from the photolysis of 8 Torr of *n*-hexanal at 280 nm: experimental data (●) and the calculated profile (—) using the ACUCHEM simulation program.

$k_{HCO+n-C_5H_{11}}$, $k_{HCO+n-C_5H_{11}CHO}$, $k_{n-C_5H_{11}+n-C_5H_{11}}$, and $k_{n-C_5H_{11}}$) and the initial HCO concentration ($[HCO]_0$). The rate constant for the n-C_5H_{11} + n-C_5H_{11} reaction was assumed to be 2.0×10^{-11} cm^3 molecule^{-1}s^{-1}. (A $k_{C_2H_5+C_2H_5}$ and $k_{n-C_3H_7+n-C_3H_7}$ value of 2.0×10^{-11} cm^{3}molecule^{-1}s^{-1} has been reported.[37,38]) The literature $k_{n-C_5H_{11}}$ value[39] of 1.7×10^3 s^{-1} was also used. Initial values of $k_{HCO+HCO}$, $k_{HCO+n-C_5H_{11}}$, and $k_{HCO+n-C_5H_{11}CHO}$ were given to the program, and the simulated HCO profiles were compared with the experimental results. Numerical values of $k_{HCO+HCO}$, $k_{HCO+n-C_5H_{11}}$, and $k_{HCO+n-C_5H_{11}CHO}$ were subsequently adjusted to optimize the fit. Values for the extracted coefficients $k_{HCO+HCO}$, $k_{HCO+n-C_5H_{11}}$, and $k_{HCO+n-C_5H_{11}CHO}$ are $(7.1 \pm 0.6) \times 10^{-11}$, $(7.1 \pm 0.6) \times 10^{-11}$, and $(1.1 \pm 0.3) \times 10^{-14}$ cm^3 molecule^{-1} s^{-1}, respectively. The uncertainty (1σ) represents experimental scatter only. The HCO decay profiles at all three *n*-hexanal pressures are well fit by the extracted $k_{HCO+HCO}$, $k_{HCO+n-C_5H_{11}}$, and $k_{HCO+n-C_5H_{11}CHO}$. The accuracy of the $k_{HCO+HCO}$ and $k_{HCO+n-C_5H_{11}}$ measurements is affected by the accuracy in the determination of the HCO absorption cross section (σ_{HCO}) and its initial concentration ($[HCO]_0$) and by the time resolution of the cavity ring-down spectroscopy (~18−31 μs around 613 nm). The value of σ_{HCO} that was used in the computation was $\sim 2.0 \times 10^{-18}$ cm^2/molecule. It was derived by measuring the HCO absorption from formaldehyde photolysis, for which the recommended HCO quantum yield[31] is available at each photolysis wavelength. We had previously reported σ_{HCO} in the range of 1.6×10^{-18} to 2.0×10^{-18} cm^2/molecule at 613.8 nm using the same cavity ring-down setup.[9] The initial HCO concentration was in the range of 8.1×10^{12} to 1.1×10^{13} molecules cm^{-3} when *n*-hexanal pressure was varied between 4 and 8 Torr. (The detection sensitivity toward HCO radicals at 280 nm was about 3.2×10^{11} molecules cm^{-3} for a 2-mm-wide photolysis beam; the initial aldehyde concentration that was used was rather high in order to operate under the condition of high signal-to-noise ratio.) The overall uncertainty for the extracted $k_{HCO+HCO}$ and $k_{HCO+n-C_5H_{11}}$ is about 50%. The value of $k_{HCO+HCO}$ agrees well with the recommended rate constant[31] for the HCO + HCO reaction (2.5×10^{-11} to 10.0×10^{-11} cm^3 molecule^{-1} s^{-1} at 300 K). The size of $k_{HCO+n-C_5H_{11}}$ is in line with those reported previously for the HCO + C_2H_5 reaction[37] (7.2×10^{-11} cm^3 molecule^{-1} s^{-1}) and the HCO + n-C_3H_7 reaction[37] (6.5×10^{-11} cm^3 molecule^{-1} s^{-1}). The influence of the numerical value of $k_{HCO+n-C_5H_{11}CHO}$ on the HCO decay profile becomes important for the time scale on the order of hundreds of microseconds. Because the HCO decay profiles were measured at several *n*-hexanal pressures under the condition that $[HCO]_0 \ll [n\text{-}C_5H_{11}CHO]_0$, the overall uncertainty in the value of $k_{HCO+n-C_5H_{11}CHO}$ is ~30%. Because of the lower vapor pressure of *n*-heptanal (~2.3 Torr at 293 K) and, as a result, a smaller HCO signal size, we have not attempted to measure the HCO + HCO, HCO + n-C_6H_{13}, and HCO + n-$C_6H_{13}CHO$ rate constants from the photolysis of *n*-heptanal.

HCO Quantum Yields from the Photolysis of *n*-Hexanal and *n*-Heptanal in the 280−330-nm Region. The HCO quantum yields from the photolysis of *n*-hexanal and *n*-heptanal were determined from the ratio of the HCO concentration produced in the pump/probe laser overlapping region to the absorbed photon density in the same region. The overlapping region could be viewed as a rectangular solid with the center overlapped with that of the cell, with the width and height defined by those of the photolysis beam and the length of the rectangular solid defined by (beam width) × $(\tan 15°)^{-1}$, where 15° is the crossing angle between the pump and the probe laser beams. The length of the photolysis/probe laser overlapping region is defined by (beam width) × $(\sin 15°)^{-1}$. Depending upon the identity of the laser dyes used, the photolysis beam width varied between 1.5 and 3.0 mm, and the uncertainty in the beam width measurements is about 15%. The probe laser beam width was about 1.0 mm. The length of the pump/probe laser overlapping region is between 5.8 ± 0.8 and 11.6 ± 1.9 mm. The photolysis beam is absorbed by *n*-hexanal or *n*-heptanal over the entire level arm through which it travels. The absorbed photolysis photon density in the pump/probe laser overlapping region could be derived from the difference in the transmitted photolysis beam energy entering (E_{in}) and leaving (E_{out}) that region, the individual photon energy (hc/λ) at the photolysis wavelength (λ), and the volume (v) of the overlapping region by using the following equations

$$\text{absorbed photon density} = \frac{E_{in} - E_{out}}{h\frac{c}{\lambda}v}$$

$$v = \text{beam width} \times \text{beam height} \times \text{length of the rectangular solid}$$

$$= \text{beam width} \times \text{beam height} \times (\text{beam width}) \times (\tan 15°)^{-1}$$

The photolysis beam energy entering or leaving the pump/probe laser overlapping region can be calculated from the incident photolysis beam energy entering the cell (E_0), the absorption cross section (σ), the density (n) of the aldehyde in the cell, and the absorbing path length by applying Beer's law

$$E_{in} = E_0 \exp(-\sigma n l_1)$$

$$E_{out} = E_0 \exp(-\sigma n l_2)$$

where l_1 is the distance between the photolysis beam entrance and the beginning of the pump/probe laser overlapping region and l_2 is the distance between the photolysis beam entrance and the end of the pump/probe laser overlapping region. The incident photolysis beam energy was measured by a calibrated joulemeter placed in front of the cell. The incident beam energy inside the cell was corrected for transmission loss at the front cell window

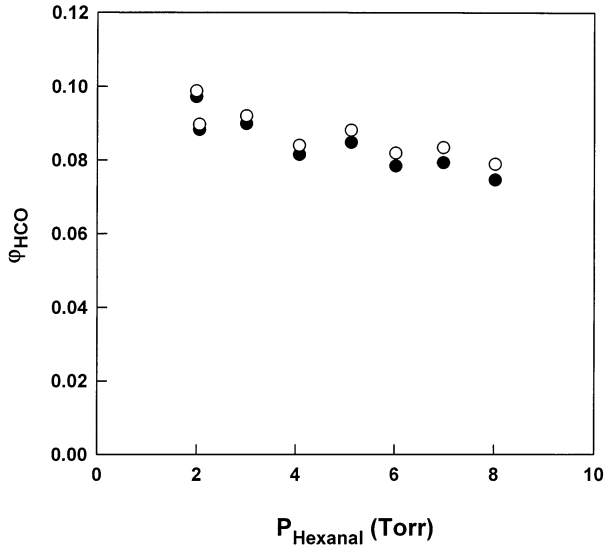

Figure 4. HCO quantum yields as a function of *n*-hexanal pressure at the 300-nm photolysis wavelength: uncorrected yields (●) and yields (○) that have been corrected for HCO radical reactions at 15 μs.

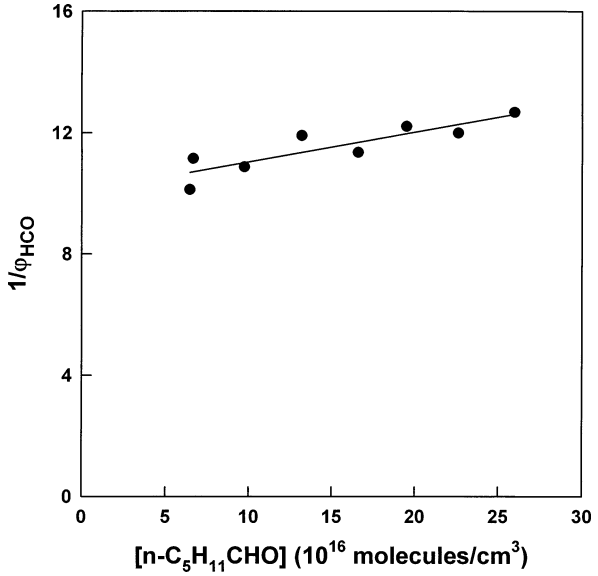

Figure 5. Reciprocal HCO quantum yields as a function of *n*-hexanal concentration at the 300-nm photolysis wavelength. The solid line is a fit of experimental data to the Stern−Volmer equation.

and for reflection of the photolysis beam from the rear cell window. The HCO concentration after the photolysis was obtained by measuring its absorption at 613.80 nm at a photolysis and a probe laser delay of 15 μs. To convert HCO absorption into absolute concentration, the absorption cross section of HCO at the probe laser wavelength was determined relative to that from the formaldehyde photolysis, HCHO + $h\nu$ → HCO + H, for which the recommended HCO quantum yield at each photolysis wavelength is available.[31] Because the precision of our HCO concentration calibration depends on the precision of the HCO yield from the formaldehyde photolysis, our result will scale with this yield. HCHO was produced immediately prior to each calibration run in a glass bulb. The HCHO absorption cross section was determined by measuring the transmitted photolysis photon fluence as a function of HCHO pressure in the cell and by applying Beer's law to the obtained data. Because the HCO absorption was measured 15 μs after the photolysis of HCHO, the following sequence of reactions has been used to calculate the HCO concentration at t = 15 μs (about 1−4% correction between the nascent HCO concentration and the HCO concentration at t = 15 μs for formaldehyde pressure in the 1−3 Torr range; $[HCO]_0$ was calculated from the absorbed photon density in the pump/probe laser overlapping region and from the recommended HCO yields from the HCHO photolysis[31]).

$$HCO + HCO \rightarrow HCHO + CO \quad (7)$$

$$H + HCO \rightarrow H_2 + CO \quad (12)$$

$$H + HCHO \rightarrow H_2 + HCO \quad (13)$$

The $k_{HCO+HCO}$ value of 7.1 × 10^{-11} cm^3 molecule^{-1} s^{-1} determined from this work was used in the fit. The literature k_{H+HCO} and k_{H+HCHO} values of 1.5 × 10^{-10} and 3.8 × 10^{-14} cm^3 molecule^{-1} s^{-1} were also used in the simulation.[40]

The dependence of the HCO radical quantum yields on *n*-hexanal and *n*-heptanal pressures was measured. The pressure of *n*-hexanal was varied between 0.5 and 8 Torr, and that of *n*-heptanal was varied between 0.5 and 4 Torr. Displayed in Figure 4 is a plot of the HCO quantum yields (φ_{HCO}) as a function of *n*-hexanal pressure at a photolysis wavelength of 300 nm. The HCO radical yields decrease with increasing *n*-hexanal pressure possibly because of the quenching of the excited *n*-hexanal by the ground-state *n*-hexanal molecules and the increasing HCO + HCO, HCO + *n*-C_5H_{11}, and HCO + *n*-$C_5H_{11}CHO$ reactions at higher *n*-hexanal pressures. To separate the contribution of HCO radical reactions from that of the quenching, we have corrected the HCO radical yields for HCO radical reactions at 15 μs (about 0.4−6% correction for *n*-hexanal pressure in the 0.5−8 Torr range) and have included in Figure 4 both the uncorrected and corrected HCO radical yields. The corrected HCO quantum yields still decrease with increasing *n*-hexanal pressure at 300 nm, suggesting an aldehyde pressure quenching effect. The corrected reciprocal HCO quantum yields were plotted against *n*-hexanal concentration ([*n*-$C_5H_{11}CHO$]) according to the Stern−Volmer equation

$$\frac{1}{\varphi_{HCO}} = \frac{1}{\varphi^0_{HCO}} + \frac{k^Q_{n-C_5H_{11}CHO}}{k^D_{n-C_5H_{11}CHO}}[n - C_5H_{11}CHO]$$

where φ^0_{HCO} is the HCO quantum yield extrapolated to zero aldehyde pressure and $k^Q_{n-C_5H_{11}CHO}/k^D_{n-C_5H_{11}CHO}$ is the ratio of quenching to the unimolecular decay rate constant of the excited *n*-hexanal. Shown in Figure 5 is a plot of $1/\varphi_{HCO}$ versus [*n*-$C_5H_{11}CHO$] at a photolysis wavelength of 300 nm; it is linear. Experimentally derived φ^0_{HCO} and k^Q/k^D from the photolysis of *n*-hexanal and *n*-heptanal as a function of photodissociation wavelength are listed in Table 2 and plotted in Figure 6 (φ^0_{HCO} only). It can be seen from Figure 6 that the zero-pressure HCO quantum yields from *n*-hexanal and *n*-heptanal photolysis exhibit significant wavelength dependencies and decrease at both the longer and the shorter-wavelength ends. The decrease in HCO quantum yields with decreasing wavelength at the shorter wavelength end can possibly be attributed to the opening of an additional photolysis pathway, such as the formation of RH + CO (R = *n*-C_5H_{11} for *n*-hexanal and R = *n*-C_6H_{13} for *n*-heptanal), at higher photon energies. The reduced HCO quantum yields at the longer-wavelength end may be the result of dissociation at near-threshold wavelengths. The peak HCO quantum yield from *n*-hexanal photolysis is 0.15 ± 0.02, and that from *n*-heptanal photolysis is 0.15 ± 0.06. A similar peak

TABLE 2: Values of φ^0_{HCO} and k^Q/k^D from the Photolysis of *n*-Hexanal and *n*-Heptanal

λ (nm)	φ^0_{HCO} (*n*-hexanal)	k^Q/k^D (*n*-hexanal; 10^{-18} cm^2)	φ^0_{HCO} (*n*-heptanal)	k^Q/k^D (*n*-heptanal; 10^{-17} cm^2)
280	0.073 ± 0.007	6.8 ± 2.1	0.081 ± 0.013	3.3 ± 0.6
285	0.091 ± 0.017	10.0 ± 2.9	0.090 ± 0.011	4.8 ± 2.3
290	0.089 ± 0.011	8.7 ± 2.5	0.098 ± 0.016	4.3 ± 2.0
295	0.10 ± 0.01	7.0 ± 0.5	0.12 ± 0.03	5.1 ± 3.3
300	0.088 ± 0.006	9.4 ± 2.7	0.11 ± 0.03	8.0 ± 3.5
305	0.12 ± 0.01	9.3 ± 2.4	0.14 ± 0.04	7.8 ± 2.2
310	0.15 ± 0.02	14.5 ± 5.4	0.15 ± 0.06	11.0 ± 5.9
315	0.14 ± 0.02	15.8 ± 3.5	0.10 ± 0.01	10.9 ± 6.2
320	0.10 ± 0.01	13.0 ± 4.9	0.11 ± 0.02	11.3 ± 3.3
325	0.095 ± 0.018	20.0 ± 7.7	0.10 ± 0.02	14.0 ± 3.0
330	0.079 ± 0.024	22.0 ± 15.0	0.098 ± 0.026	8.9 ± 3.7

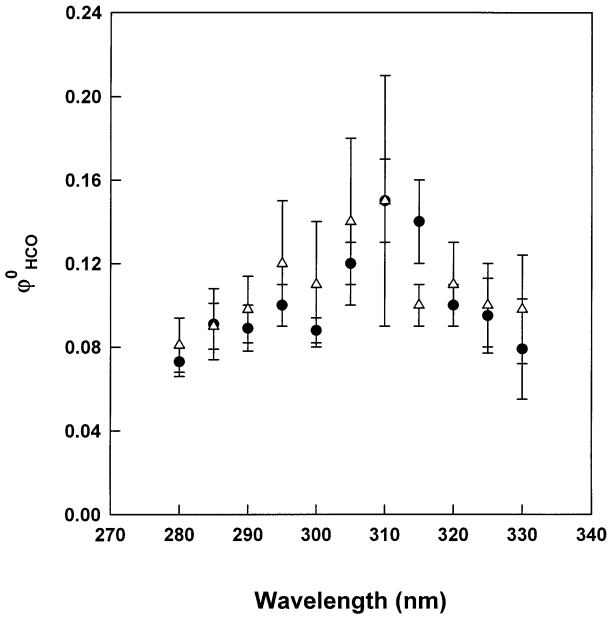

Figure 6. Zero-pressure HCO quantum yields as a function of photolysis wavelength for *n*-hexanal (●) and *n*-heptanal (△).

HCO quantum yield was also obtained from *n*-pentanal photolysis.[10] Thus, it appears that the peak HCO quantum yield from aldehyde photolysis does not vary with alkyl chain length for aldehydes with a chain length longer than or equal to five carbon atoms. Error bars were obtained using cumulative error analysis of the standard deviations of at least two $1/\varphi_{HCO}$ versus [RCHO] plots. Systematic errors contain uncertainties in the determination of the following parameters: HCO absorption cross section (∼20%), *n*-hexanal or *n*-heptanal concentration and absorption cross section (∼10% for *n*-hexanal and ∼15% for *n*-heptanal), pulse energy (∼5%), the angle between the photolysis and the probe lasers (3%), and the dye-laser width. Because the HCO quantum yields from the photolysis of *n*-hexanal and *n*-heptanal were determined relative to those obtained from HCHO photolysis, the uncertainty in the dye-laser width measurement should not directly affect the relative HCO quantum yields, but it will affect the correction of the HCO radical reactions. As a result, uncertainty in the dye-laser width measurement will indirectly affect the yield data. Adding the relative (7%−30% for *n*-hexanal and 10−40% for *n*-heptanal) and the systematic errors, the overall uncertainty in the determination of φ^0_{HCO} over the wavelength range studied is about 45−68% for *n*-hexanal and about 53−83% for *n*-heptanal.

The dependence of the HCO radical quantum yields on total pressure was examined by keeping a constant *n*-hexanal or *n*-heptanal pressure and changing the nitrogen buffer gas pressure. The HCO radical quantum yields were found to be independent of total pressure (6−387 Torr) to within the experimental error limit in the 280−330-nm region. In the presence of excess nitrogen, an inefficient electronic-to-rotational/translational energy transfer ($E \rightarrow {}^R/_T$) and a vibrational-to-rotational/translational energy transfer ($V \rightarrow {}^R/_T$) between the vibronically excited *n*-hexanal or *n*-heptanal and nitrogen could occur. When several Torr of *n*-hexanal or *n*-heptanal is photolyzed, an efficient electronic-to-vibrational energy transfer ($E \rightarrow V$) and a resonant vibrational-to-vibrational energy transfer ($V \rightarrow V$) between the excited state and the ground-state aldehyde can occur. To explain our observation of the self-quenching of *n*-hexanal and *n*-heptanal by an aldehyde pressure of several Torr but not by nitrogen pressure of several hundred Torr, we compare the quenching rate constants of vibronically excited formaldehyde by itself and by nitrogen because the corresponding quenching rate constants are not available for *n*-hexanal and *n*-heptanal. The vibrational and electronic energy removal rate constants for H_2CO ($\tilde{A}$, $^1A_2$) in the 4^1 level (the vibrational energy gap used was 125 cm^{-1}, $\lambda_{excitation}$ = 351.9 nm) were reported to be 6.7×10^{-10} and 0.37×10^{-10} cm^3 molecule^{-1} s^{-1} for formaldehyde as a quencher and 2.8×10^{-10} and 0.5×10^{-12} cm^3 molecule^{-1} s^{-1} for nitrogen as a quencher.[41] Thus, the vibronic quenching of formaldehyde by itself is at least 177 times more efficient than that by nitrogen. By analogy, the collisional vibronic quenching of *n*-hexanal and *n*-heptanal by nitrogen can be very inefficient compared with their self-quenching. It is not surprising that we did not observe pressure quenching of *n*-hexanal and *n*-heptanal by nitrogen at the limited nitrogen-pressure range in which we operated ($P_{total} \leq 387$ Torr). If we were able to operate at nitrogen pressures of several thousand Torr or higher, then we might observe quenching of *n*-hexanal or *n*-heptanal by nitrogen. For atmospheric purposes, we feel that it is a good approximation to set the zero-pressure HCO quantum yields from the photolysis of *n*-hexanal and *n*-heptanal equal to those in the presence of 760 Torr of nitrogen because nitrogen is an extremely poor quencher of vibronically excited *n*-hexanal and *n*-heptanal.

One might wonder if the aldehyde pressure dependence of the HCO signal could be caused by multiexponential decay in the cavity ring-down signal that can lead to nonlinear absorption measurements at higher aldehyde pressure. We did not observe multiexponential decay in the cavity ring-down signal, even at the highest aldehyde pressure used. The round-trip HCO absorption was small, even at the highest *n*-hexanal and *n*-heptanal pressure used. For example, the round-trip HCO absorption was less than 27 ppm at 8 Torr *n*-hexanal pressure for nearly all photolysis wavelengths. We believe the cause for the reduced HCO signal at higher aldehyde pressure is the effect of quenching.

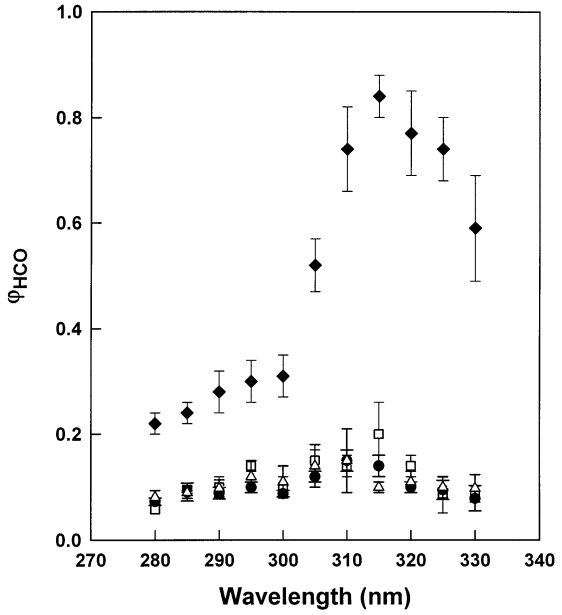

Figure 7. HCO quantum yields as a function of wavelength from the photolysis of *n*-butanal (◆, ref 9), *n*-pentanal (□, ref 10), *n*-hexanal (●, this work), and *n*-heptanal (△, this work).

Tadić and co-workers[24] investigated the photooxidation of *n*-hexanal in air by combining fluorescent UV-lamp photolysis (275−380 nm) with the detection of end products with FTIR. Major products that were analyzed include 1-butene, CO, vinyl alcohol, and acetaldehyde. Two photodecomposition channels were identified: the radical channel (C_5H_{11} + HCO) and the Norrish II channel ($C_4H_8 + CH_2{=}CHOH \leftrightarrow C_4H_8 + CH_3CHO$). The yield of the radical or Norrish II channel was obtained from the ratio of the amount of CO or 1-butene that was formed to the amount of *n*-hexanal that was photolyzed. The relative yield of the radical channel versus the Norrish II channel was 27%: 73%. The absolute photolysis quantum yield was 0.43 in 100 Torr of air and 0.38 in 700 Torr of air. Both the HCO + C_5H_{11} channel and the CO + C_5H_{12} channel are sources of CO when *n*-hexanal is photolyzed in air. Because the relative contributions of the HCO + C_5H_{11} channel and the CO + C_5H_{12} channel are not known, a direct comparison with our HCO yield is not possible. Our HCO yield from *n*-hexanal photolysis averaged over the 280−330-nm region is 0.10. We did not observe a dependence of the HCO yield on nitrogen buffer gas pressure in the 6−387 Torr range.

Tadić and co-workers[26] also studied the photooxidation of *n*-heptanal in air by using UV-lamp photolysis (275−380 nm) with FTIR. The main products that were identified include 1-pentene, CO, vinyl alcohol, and acetaldehyde. The absolute photolysis quantum yields were found to be slightly dependent on the total pressure. They were 0.36 ± 0.03 in 100 Torr of air and 0.31 ± 0.01 in 700 Torr of air. The two decomposition channels that were identified were the radical channel (C_6H_{13} + HCO) and the Norrish II channel ($C_5H_{10} + CH_2{=}CHOH \leftrightarrow C_5H_{10} + CH_3CHO$), having absolute quantum yields of 0.031 and 0.118, respectively, at 700 Torr. Our HCO radical yield from *n*-heptanal photolysis averaged over the 280−330-nm region is 0.11. We did not observe the dependence of the HCO yield on nitrogen buffer gas pressure.

Comparison with the Photolysis of Other Aldehydes. The photolysis of *n*-hexanal and *n*-heptanal is compared with the photolysis of *n*-butanal[9] and *n*-pentanal.[10] Shown in Figure 7 are the HCO radical quantum yields as a function of wavelength from the photolysis of *n*-butanal, *n*-pentanal, *n*-hexanal, and *n*-heptanal. The shape of the HCO quantum yields versus the wavelength curve and the magnitude of the HCO radical yields are similar for *n*-pentanal, *n*-hexanal, and *n*-heptanal. The peak HCO radical yields decrease with increasing chain length when going from *n*-butanal to *n*-pentanal, but this decreasing trend does not continue for aldehydes with chain lengths longer than or equal to five carbon atoms. Because *n*-pentanal, *n*-hexanal, and *n*-heptanal have γ or δ hydrogen atoms that can be readily abstracted intramolecularly by the O atom to form Norrish type II photoelimination products or to form the photocyclization products, similar yields of intramolecular isomerization products can be expected from the photolysis of these longer-chain aldehydes. As a result, similar HCO radical yields can be expected from the photolysis of aldehydes with chain lengths of five carbon atoms or longer. However, *n*-butanal has only primary γ hydrogen atoms, which are less reactive than secondary γ hydrogen atoms; therefore, radical formation is the preferred process from *n*-butanal photolysis.

End-Product Studies with Mass Spectrometry and FTIR. *n*-Hexanal and *n*-heptanal were photolyzed in a closed cell by a 308-nm excimer laser. The photolysis end products were analyzed by a residual gas analyzer mass spectrometer and an FTIR. A summary of the product yields obtained from the end-product study is given in Table 3. Presented in Figure 8 are mass spectra with and without photolyzing 2.8 Torr of *n*-hexanal in the cell. Given in Figure 9 is an amplified differential spectrum that was obtained from the subtraction of the two mass spectra shown in Figure 8. As can be seen, mass spectra peak intensity at m/e = 30, 32, 46, 54, 56, 68, 71, and 83 increases after the photolysis. The m/e = 30 peak in Figure 9 would correlate with HCHO product formed from the self-reaction of the photolytically generated HCO radicals. Mass spectral peaks at m/e = 32, 68, and 83 would correlate with a photocyclization product such as 2-methylcyclopentanol from *n*-hexanal photolysis

$$C_5H_{11}CHO + h\nu \rightarrow \text{2-methylcyclopentanol} \qquad (5)$$

Mass spectral peaks at m/e = 46, 54, 71, and 83 would probably correlate with a photocyclization product such as 2-ethylcyclobutanol from *n*-hexanal photolysis

$$C_5H_{11}CHO + h\nu \rightarrow \text{2-ethylcyclobutanol} \qquad (6)$$

The m/e = 56 peak would correlate with the 1-butene photoproduct. From the mass spectra of *n*-hexanal with and without photolysis and using standards of 1-butene and 2-methylcyclopentanol to calibrate the products' mass spectra, we obtained estimates of the yields of the Norrish II, 2-methylcyclopentanol, and 2-ethylcyclobutanol channels from the 308-nm photolysis of *n*-hexanal, which are 0.28 ± 0.04, 0.12 ± 0.02, and 0.30 ± 0.11, respectively. Hansen and Lee[25] measured the 1-butene yields from the photolysis of *n*-hexanal at 254 and 312 nm. They were 0.26 ± 0.03 and 0.23 ± 0.03 at 254 and 312 nm, respectively. Our 1-butene yield of 0.28 ± 0.04 at the 308-nm photolysis wavelength is in line with those reported previously by Hansen and Lee. When *n*-heptanal was photolyzed at 308 nm, products such as HCHO, 1-pentene, 2-methylcyclohexanol, and 2-ethylcyclopentanol were detected by mass spectrometry. The sum of the yields of the 2-methylcyclohexanol channel and the 2-ethylcyclopentanol channel is 0.40 ± 0.04. The yield of the Norrish II channel is estimated to be 0.26 ± 0.02.

The photolysis precursors and products from the 308-nm excimer laser photolysis of *n*-hexanal were transferred to a 10-m White cell and analyzed by a Bruker IFS66v FTIR spectrometer.

TABLE 3: End-Product Yields from 308-nm Photolysis of *n*-Hexanal and *n*-Heptanal

		quantum yield	
reactant	photolysis channel	mass spectrometry	FTIR
n-hexanal	$CH_3CHO + C_4H_8$	0.28 ± 0.04	0.31 ± 0.03
	$CO + C_5H_{12}$		0.20 ± 0.07[a]
	$HCO + C_5H_{11}$		0.34 ± 0.07
	2-methylcyclopentanol	0.12 ± 0.02	
	2-ethylcyclobutanol	0.42 ± 0.11	
n-heptanal	$CH_3CHO + C_5H_{10}$	0.26 ± 0.02	0.27 ± 0.03
	$CO + C_6H_{14}$		0.23 ± 0.09[a]
	$HCO + C_6H_{13}$		0.38 ± 0.07
	2-methylcyclohexanol		
	2-ethylcyclopentanol	0.40 ± 0.04	

[a] Yield for the CO + RH channel was obtained by subtracting the yield of the R + HCO channel obtained from the ring-down measurements from the total CO yields obtained from FTIR measurements.

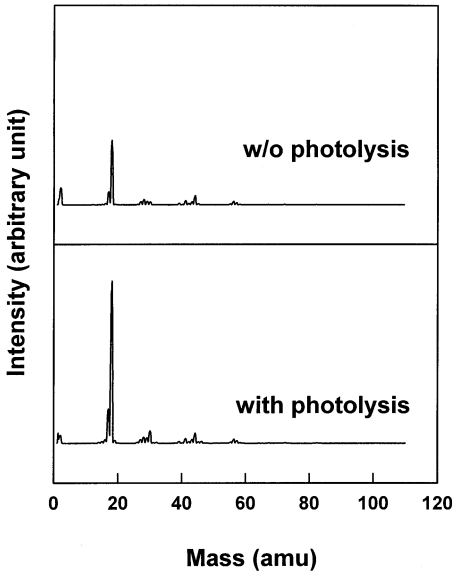

Figure 8. Mass spectra of *n*-hexanal with and without photolysis at the 308-nm excimer laser wavelength. The *n*-hexanal pressure in the photolysis cell is 2.8 Torr.

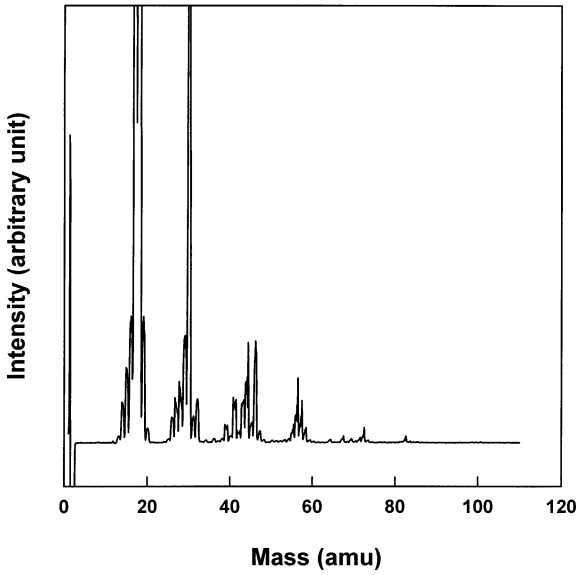

Figure 9. Difference in the mass spectra shown in Figure 8.

Provided in Figure 10 are FTIR spectra of *n*-hexanal before and after the photolysis and the difference spectrum. The infrared spectra were taken at a spectral resolution of 0.5 cm^{-1}. The minus signal in the difference spectrum corresponds to a decrease in the infrared absorption of *n*-hexanal as a result of photodissociation. The major products were identified to be CO (2040−2250 cm^{-1}), 1-butene (912, 1648, and 3089 cm^{-1}), vinyl alcohol (1100 and 1254 cm^{-1}), acetaldehyde (1350−1355 cm^{-1}), and CO_2 (2280−2380 cm^{-1}). Carbon monoxide is most likely a product of the HCO + C_5H_{11} and CO + C_5H_{12} photodissociation channels. After subtracting the HCO radical yield (0.14 ± 0.02) at 308 nm that was obtained from our cavity ring-down study, the yield of the CO + C_5H_{12} channel is estimated to be 0.20 ± 0.07 at the 308-nm photolysis wavelength. We also attempted to determine the yield of the CO + C_5H_{12} channel by monitoring the infrared absorption of the C_5H_{12} product, but its overlapping absorption with *n*-hexanal prevented us from obtaining a C_5H_{12} product yield using this method. 1-Butene, vinyl alcohol, and acetaldehyde are products

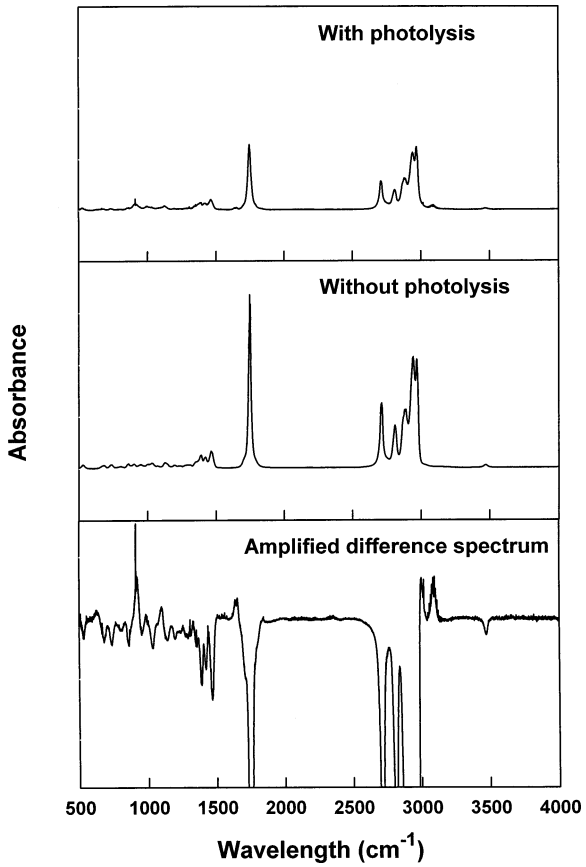

Figure 10. FTIR spectra of *n*-hexanal with and without 308-nm photolysis irradiation and the difference spectrum. The *n*-hexanal pressure in the photolysis cell is 0.27 Torr.

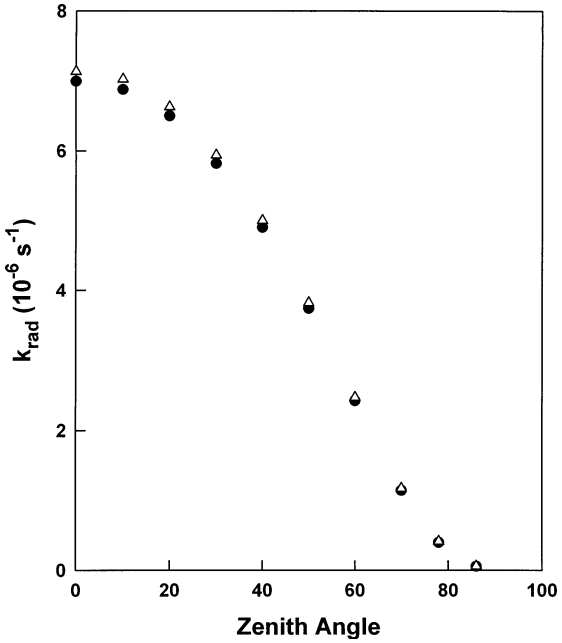

Figure 11. Atmospheric HCO radical-formation rate constants from the photolysis of *n*-hexanal (●) and *n*-heptanal (△) as a function of zenith angle at 760 Torr of nitrogen pressure.

that can be expected from the Norrish II channel. By monitoring the amount of 1-butene formed and the amount of *n*-hexanal photodissociated, we estimated the yield of the Norrish II channel from the 308-nm photolysis of *n*-hexanal to be 0.31 ± 0.03. CO_2 is probably an artifact resulting from reactions at the wall. Because there was an overlap between the infrared absorption peaks of 2-methylcyclopentanol and 2-ethylcyclobutanol and those of *n*-hexanal, the presence of photocyclization products in the infrared spectra can be obscured because of this overlap in absorption. That was probably the reason that the previous smog chamber/FTIR study[24] did not observe the photocyclization product from *n*-hexanal photolysis. When *n*-heptanal was photolyzed by a 308-nm excimer laser, the major products observed by FTIR included CO (2040−2230 cm^{-1}), 1-pentene (913, 1461, 1646, 3088 cm^{-1}), vinyl alcohol (1100, 1242, 1266 cm^{-1}), acetaldehyde (1349−1355 cm^{-1}), and CO_2 (2270−2390 cm^{-1}). The estimated yields of the CO + C_6H_{14} channel and the Norrish II channel from 308-nm excimer-laser photolysis of *n*-heptanal are 0.23 ± 0.09 and 0.27 ± 0.03, respectively.

Photodissociation Rate Constants for Forming HCO Radicals in the Atmosphere. The atmospheric radical formation rate constants (k_{rad}) from the photolysis of *n*-hexanal and *n*-heptanal were calculated using the actinic solar flux ($J(\lambda)$) reported by Demerjian and co-workers;[42] the absorption cross sections of *n*-hexanal and *n*-heptanal ($\sigma(\lambda)$), and the HCO radical quantum yield at 760 Torr nitrogen pressure ($\varphi_{HCO}(\lambda)$) using the relationship

$$k_{rad} = \Sigma\sigma(\lambda)\,\varphi_{HCO}(\lambda)J(\lambda)\Delta\lambda$$

Radical-formation rate constants from the photodissociation of *n*-hexanal and *n*-heptanal were estimated as a function of the zenith angle under cloudless conditions at sea level and for best-estimate albedo (5% in the 290−330-nm region[43]); the results are shown in Figure 11. Our estimated HO_x radical-production rate constants for zenith angles in the 30−60° range are 5.8 × 10^{-6} to 2.4 × 10^{-6} s^{-1} for *n*-hexanal and 5.9 × 10^{-6} to 2.5 × 10^{-6} s^{-1} for *n*-heptanal. The OH radical production rate constants from ozone photolysis followed by the $O(^1D)/H_2O$ reaction are about 66.2 × 10^{-6} to 14.6 × 10^{-6} s^{-1} for zenith angles in the 30−60° range. Because the radical production capability is similar for aliphatic aldehydes with chain lengths longer than four carbon atoms, their photodissociation can be a significant source of HO_x radicals in the polluted, VOC-rich atmospheric environments. Assuming a photolysis quantum yield of unity in the actinic UV region for *n*-hexanal and *n*-heptanal, their corresponding atmospheric photodissociation lifetimes are on the order of 4.5−12.6 and 4.4−12.3 h for zenith angles in the 0−60° range. Rate constants[44,45] for OH-radical reactions with *n*-hexanal and *n*-heptanal have been reported to be 2.6 × 10^{-11} and 3.0 × 10^{-11} cm^3 $molecule^{-1}$ s^{-1}, respectively, which correspond to OH-radical reaction lifetimes of 5.3 and 4.6 h for the average noontime OH concentration[26] of 2 × 10^6 cm^{-3}. Therefore, both photolysis and the OH-radical reaction are important removal pathways for *n*-hexanal and *n*-heptanal in the atmosphere.

Acknowledgment. We thank Ms. Sarani Datta for her assistance with the experiments. Helpful discussions with Dr. Liang T. Chu are acknowledged. We are grateful for the support provided by the National Science Foundation under grant no. ATM-0300294. Any opinions, findings, and conclusions expressed in this paper are those of the authors and do not necessarily reflect the views of the National Science Foundation.

References and Notes

(1) Vairavamurthy, A.; Roberts, J. M.; Newman, L. *Atmos. Environ., Part A* **1992**, *26*, 1965.
(2) Carlier, P.; Hannachi, H.; Mouvier, G. *Atmos. Environ.* **1986**, *20*, 2079.
(3) Finlayson-Pitts, B. J.; Pitts, J. N., Jr. *Atmospheric Chemistry*; John Wiley & Sons: New York, 1986.
(4) Moortgat, G. K.; Seiler, W.; Warneck, P. *J. Chem. Phys.* **1983**, *78*, 1185.
(5) Carmely, Y.; Horowitz, A. *Int. J. Chem. Kinet.* **1984**, *16*, 1585.
(6) Ho, P.; Bamford, D. J.; Buss, R. J.; Lee, Y. T.; Moore, C. B. *J. Chem. Phys.* **1982**, *76*, 3630.
(7) Horowitz, A.; Calvert, J. G. *J. Phys. Chem.* **1982**, *86*, 3105.
(8) Chen, Y.; Zhu, L. *J. Phys. Chem. A* **2001**, *105*, 9689.
(9) Chen, Y.; Zhu, L.; Francisco, J. S. *J. Phys. Chem. A* **2002**, *106*, 7755.
(10) Cronin, T. J.; Zhu, L. *J. Phys. Chem. A* **1998**, *102*, 10274.
(11) Ciccioli, P.; Brancaleoni, E.; Frattoni, M.; Cecinato, A.; Brachetti, A. *Atmos. Environ., Part A* **1993**, *27*, 1891.
(12) Owen, S.; Boissard, C.; Street, R. A.; Duckham, S. C.; Csiky, O.; Hewitt, C. N. *Atmos. Environ.* **1997**, *31* (SI), 101.
(13) Kirstine, W.; Galbally, I.; Ye, Y.; Hooper, M. *J. Geophys. Res.* **1998**, *103*, 10605.
(14) Karl, T.; Guenther, A.; Lindinger, C.; Jordan, A.; Fall, R.; Lindinger, W. *J. Geophys. Res.* **2001**, *106*, 24157.
(15) Karl, T.; Fall, R.; Jordan, A.; Lindinger, W. *Environ. Sci. Technol.* **2001**, *35*, 2926.
(16) Fall, R.; Karl, T.; Jordan, A.; Lindinger, W. *Atmos. Environ.* **2001**, *35*, 3905.
(17) Grosjean, D.; Grosjean, E.; Gertler, A. W. *Environ. Sci. Technol.* **2001**, *35*, 45.
(18) Kean, A. J.; Grosjean, E.; Grosjean, D.; Harley, R. A. *Environ. Sci. Technol.* **2001**, *35*, 4198.
(19) Schauer, J. J.; Kleeman, M. J.; Cass, G. R.; Simoneit, B. R. T. *Environ. Sci. Technol.* **2001**, *35*, 1716.
(20) Schauer, J. J.; Kleeman, M. J.; Cass, G. R.; Simoneit, B. R. T. *Environ. Sci. Technol.* **2002**, *36*, 567.
(21) Grosjean, E.; Grosjean, D.; Seinfeld, J. H. *Environ. Sci. Technol.* **1996**, *30*, 1038.
(22) Grosjean, E.; Grosjean, D. *Environ. Sci. Technol.* **1996**, *30*, 1321.
(23) Hasson, A. S.; Ho, A. W.; Kuwata, K. T.; Paulson, S. E. *J. Geophys. Res.* **2001**, *106*, 34143.
(24) Tadić, J.; Juranić, I.; Moortgat, G. K. *Molecules* **2001**, *6*, 287.
(25) Hansen, D. A.; Lee, E. K. C. *J. Am. Chem. Soc.* **1973**, *95*, 7900.
(26) Tadić, J. M.; Juranić, I. O.; Moortgat, G. K. *J. Chem. Soc., Perkin Trans.* **2002**, *2*, 135.
(27) Martinez, R. D.; Buitrago, A. A.; Howell, N. W.; Hearn, C. H.; Joens, J. A. *Atoms. Environ., Part A* **1992**, *26*, 785.

(28) Calvert, J. G.; Pitts, J. N., Jr. *Photochemistry*; Wiley: New York, 1966.
(29) O'Keefe, A.; Deacon, D. A. G. *Rev. Sci. Instrum*. **1988**, *59*, 2544.
(30) O'Keefe, A.; Scherer, J. J.; Cooksy, A. L.; Sheeks, R.; Heath, J.; Saykally, R. J. *Chem. Phys. Lett.* **1990**, *172*, 214.
(31) Atkinson, R.; Baulch, D. L.; Cox, R. A.; Hampson, R. F., Jr.; Kerr, J. A.; Troe, J. *J. Phys. Chem. Ref. Data* **1992**, *21*, 1125.
(32) Zhu, L.; Cronin, T.; Narang, A. *J. Phys. Chem. A* **1999**, *103*, 7248.
(33) Zhu, L.; Johnston, G. *J. Phys. Chem. A* **1995**, *99*, 15114.
(34) Zhu, L.; Kellis, D.; Ding, C. F. *Chem. Phys. Lett.* **1996**, *257*, 487.
(35) Stoeckel, F.; Schuh, M. D.; Goldstein, N.; Atkinson, G. H. *Chem. Phys.* **1985**, *95*, 135.
(36) Braun, W.; Herron, J. T. *ACCUCHEM/ACUPLOT*; computer program for modeling complex reaction systems; National Bureau of Standard: Gaithersburg, MD, 1986.
(37) Baggott, J. E.; Frey, H. M.; Lightfoot, P. D.; Walsh, R. *J. Phys. Chem.* **1987**, *91*, 3386.
(38) Adachi, H.; Basco, N. *Int. J. Chem. Kinet.* **1981**, *13*, 367.
(39) Jitariu, L. C.; Jones, L. D.; Robertson, S. H.; Pilling, M. J.; Hillier, I. H. *J. Phys. Chem. A* **2003**, *107*, 8607.
(40) Baulch, D. L.; Cobos, C. J.; Cox, R. A.; Esser, C.; Frank, P.; Just, Th.; Kerr, J. A.; Pilling, M. J.; Troe, J.; Walker, R. W.; Warnatz, J. *J. Phys. Chem. Ref. Data* **1992**, *21*, 411.
(41) Shibuya, K.; Lee, E. K. C. *J. Chem. Phys.* **1978**, *69*, 758.
(42) Demerjian, K. L.; Schere, K. L.; Peterson, J. T. *Adv. Environ. Sci. Technol.* **1980**, *10*, 369.
(43) Coulson, K. L.; Reynolds, D. W. *J. Appl. Meteorol.* **1971**, *10*, 1285.
(44) Papagni, C.; Arey, J.; Atkinson, R. *Int. J. Chem. Kinet.* **2000**, *32*, 79.
(45) Albaladejo, J.; Ballesteros, B.; Jimenez, E.; Martin, P.; Martinez, E. *Atmos. Environ.* **2002**, *36*, 3231.